Damage Leading to Ductile Fracture under High Strain-Rate Conditions

J.P. FOWLER, M.J. WORSWICK, A.K. PILKEY, and H. NAHME

Quantitative metallographic studies of damage evolution leading to ductile fracture under high strain-rate loading conditions are presented. A model material is considered, namely, leaded brass, which contains a dispersed globular lead phase that acts as void nucleation sites. Interrupted tensile split Hopkinson bar tests have been performed to capture the evolution of porosity and void aspect ratio with deformation at strain rates up to 3000 s^{-1}. Both uniaxial and notched specimen geometries were considered to allow the effects of remote stress triaxiality to be investigated. Plate impact testing has also been performed to investigate the evolution of damage under the intense tensile triaxiality and extremely high rates of deformation (10^5 s^{-1}) occurring within a spall layer. Quantitative metallographic measurements of damage within deformed specimens are used to assess predictions from a Gurson-based constitutive model implemented within an explicit dynamic finite element code. A stress-controlled void nucleation treatment is shown to capture the effect of triaxiality on damage initiation for the range of experiments considered.

I. INTRODUCTION

DUCTILE fracture occurs within plastically deforming materials through the nucleation, growth, and coalescence of voids to form crack.[1,2] This mechanism is operative under dynamic loading conditions, such as impact, when the tensile reflections of compressive stress waves from free surfaces meet to produce tensile triaxial stress states.[3] Considerable past research has investigated the component stages of ductile fracture,[4–11] however, the nature of damage accumulation under high strain-rate dynamic loading has not been investigated extensively. Under dynamic loading, material effects such as strain-rate hardening will tend to elevate ductility,[12] whereas thermal softening due to adiabatic heating can lead to premature localization.[13,14] Inertial effects can delay necking under dynamic loading[15] and play an important role in determining the void expansion rate under very high strain-rate conditions.[16–19] Material viscosity will also delay void expansion under very high rates of strain.[18,20]

This article presents results from high strain-rate mechanical testing with quantitative metallographic assessment of damage development. Leaded brass was adopted as a "model material" because it contains a dispersion of lead particles acting as well-defined void nucleation sites and has been considered in a number of previous studies of ductile fracture under quasi-static[9] and dynamic[17,21,22] conditions. Results are presented from two series of high strain-rate experiments, the tensile split Hopkinson bar (TSHB), and the planar plate impact. In the TSHB tests, uniaxial and notched tensile specimens are loaded in tension at strain rates up to 3000 s^{-1}. By varying the notch geometry, tensile triaxialities in the range of 1/3 to 1.0 are achieved. Momentum trapping techniques[21,23] were applied to arrest deformation at predetermined strain levels prior to fracture, allowing construction of damage histories from a series of interrupted TSHB experiments. In the plate impact experiments, tensile triaxiality levels of 4 to 5 are generated under strain rates of 10^5 s^{-1}. Experiments were performed in which the impact velocity was reduced to just produce an incipient spall layer, that is, a layer of damage without final crack coalescence.

Quantitative metallographic measurements of porosity and void aspect ratio development were acquired over the entire gage region of the specimens interrupted prior to fracture. These measurements provided the distribution of damage within the specimens. By combining results from the series of specimens tested, histories of damage development with strain and triaxiality were constructed. Estimates for the conditions at void coalescence are obtained based on measurements from specimens interrupted close to the fracture strain. Bulk field porosity values were acquired along with detailed interparticle/void spacing statistics as inferred from interparticle dilational spacing spectra (IPDS).[24,25] These data provide insight into the progression of damage within the particle field and the role of clustered particles in initiating the void coalescence process. One interesting feature of the TSHB momentum trapping technique is the ability to interrupt deformation after the onset of mechanical instability. Under quasi-static loading, the compliance of the test frame usually prevents recovery of samples past this instability strain and prohibits metallographic study of void coalescence behavior. However, interrupted TSHB experiments enable measures of damage to be collected from incipiently fractured specimens in which extensive void coalescence has occurred.

J.P. FOWLER, formerly Research Associate with the Mechanical and Aerospace Engineering Department, Carleton University, is with the Defence Research Establishment, Suffield, P.O. Box 4000, Medicine Hat, Alberta, T1A 8K6, Canada. M.J. WORSWICK, Associate Professor, is with the Department of Mechanical Engineering, University of Waterloo, Waterloo, ON, Canada N2L 3G1. A.K. PILKEY, Assistant Professor, is with the Mechanical and Aerospace Engineering Department, Carleton University, Department of Mechanical Engineering, 1125 Colonel By Drive, Ottawa, Ontario, K1S 5B6, Canada. H. NAHME, Scientist, is with the Ernst Mach Institute, Ernst-Mach-Institut, Eckertrasse 4, 7800, Freibourg, Germany.

This article is based on a presentation given in the symposium entitled "Dynamic Behavior of Materials—Part II," held during the 1998 Fall TMS/ASM Meeting and Materials Week, October 11–15, 1998, in Rosemont, Illinois, under the auspices of the TMS Mechanical Metallurgy and the ASM Flow and Fracture Committees.

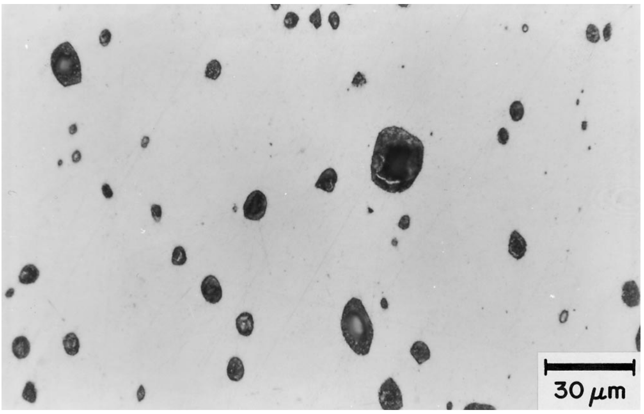

Fig. 1—Optical micrograph showing spheroidized lead phase and void damage within a notched tensile specimen. Polished only.

The measured damage histories are used to assess damage predictions obtained from a Gurson-based constitutive model[26,27,28] implemented as a user-material constitutive subroutine[29] within the LSDYNA explicit dynamic finite element code.[30] In particular, the effect of adopting a stress-controlled void nucleation model, rather than strain-controlled treatment, is examined in view of the large range of stress triaxiality and stress levels attained in the various dynamic experiments. Finally, the present high strain-rate damage results are compared with earlier quasi-static results for the leaded brass under study[9] in order to assess the influence of loading rate on damage development.

II. MATERIAL

UNS C36000 free-machining or "leaded" brass was adopted as a model material in the current study. This material, used in a number of earlier studies of ductile fracture,[9,17,21,22] has a nominal composition of 61.5 pct copper, 35.5 pct zinc, and 3 pct lead. The lead phase, added to improve machinability, is essentially insoluble in the brass matrix and forms a globular particulate phase that can be spheroidized through annealing (Figure 1). In this work, a 2-hour annealing treatment at 850 °C was employed. The measured areal fraction of lead was 0.022. During deformation, the softer lead particles burst or tear away from the brass matrix to nucleate voids, as seen in Figure 1. Due to the low strength of the lead phase in comparison to the brass matrix, it is assumed that the entire lead particle can be treated as a void after nucleation; measured porosity data reported in this article refer to the sum of the void and particle areal fractions. In this fashion, the lead phase acts as a well-defined source of spherical voids, with the geometry of the particles and their nucleated voids closely corresponding to the initially spherical void geometry assumed in many analytical models of void growth.[6,7,8,26] The darker lead phase also provides good contrast to the brass matrix for image analysis purposes.

Note that a 89-mm-diameter rod stock was used to fabricate the plate and E-notch specimens, while a 12.5-mm-diameter rod was used for the uniaxial and C-notch specimens.

III. EXPERIMENTAL PROCEDURES

Two high strain-rate experiments were performed on the leaded brass. The TSHB tests considered notched and uniaxial specimens at strain rates up to 3000 s^{-1}, while the plate impact experiments generated uniaxial strain states at rates at least one order of magnitude higher than in the tensile specimens.

A. *TSHB Experiments*

The TSHB was first developed by Harding *et al.*[31] as a variant on the original Kolsky[32] or Hopkinson[33] compression apparatus. A schematic of the TSHB used in the current work is shown in Figure 2. The cylindrical striker is accelerated by a gas gun and impacts the end of the incident bar. This impact generates a tensile stress wave that propagates down the bar and impinges on the test specimen. The specimen is generally softer and of a smaller cross-sectional area than the incident and transmitter bars so that only a portion of this wave is transmitted through the specimen as it deforms while the balance of the incident wave is reflected back along the incident bar as a compressive wave. Following the classical Hopkinson bar technique,[33] the transmitted and reflected waves are recorded using a high speed digital storage oscilloscope and are used to determine the levels of force and strain rate within the specimen *vs* time. From the force strain-rate data, the true stress-strain response of the specimen may be deduced; details of the calculations are omitted here but may be found in Reference 33.

A novel aspect of the current TSHB experiments is the addition of momentum trapping fixtures[21] based on original developments by Nemat-Nasser.[23] These fixtures consist of the incident and transmitter bar traps indicated in Figure 2. Without momentum trapping, the stress waves repeatedly reflect back and forth within the apparatus, reloading the specimen until fracture occurs. The momentum trapping

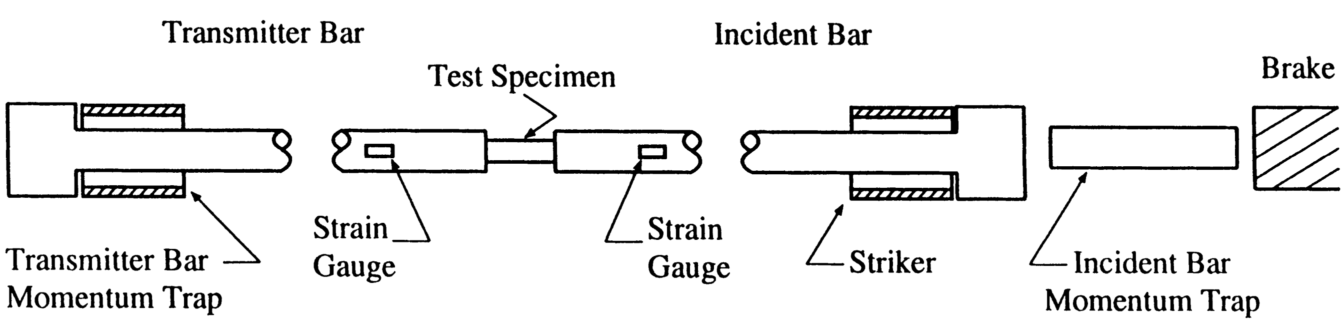

Fig. 2—Schematic of tensile split Hopkinson bar at the University of Waterloo.

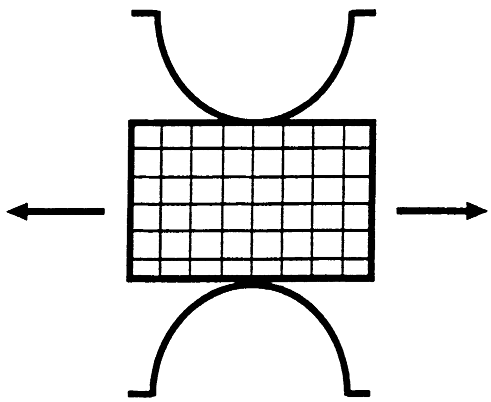

Fig. 3—Schematic of notched tensile specimen. The rectangular pattern inset within the notch region indicates the orientation of the grid pattern used to acquire damage distributions.

fixtures are used to trap the transmitted and reflected waves and prevent reloading of the specimen. The incident bar momentum trap consists of a rod of diameter equal to the incident bar and a length of 460 mm that exceeds the length of the longest striker. Prior to testing, a precision gap is set between the incident bar and the incident bar momentum trap. The size of the gap is set such that the impact of the striker upon the incident bar end cap is of sufficient duration and velocity to just close the gap. Upon reflection at the specimen, the compressive reflected wave will traverse the now-closed gap and will propagate into the momentum trap. When the reflected wave is re-reflected off the end of the momentum trap as a tensile wave, it is unable to travel back across the gap into the incident bar and is trapped. The cylindrical momentum trap positioned at the end of the transmitter bar acts in a similar fashion and traps the tensile transmitted wave.

The duration of the incident pulse is determined by the length of the striker; four strikers of lengths 102, 203, 305, and 406 mm were used. The strain rate is primarily controlled by the striker velocity. Therefore, by testing successive specimens at the same firing velocities with differing striker lengths, a series of tests can be obtained at a constant strain rate but differing levels of total strain. In this manner, the evolution of void damage with strain at high strain rates can be characterized.

In the TSHB experiments, the stress state or triaxiality, namely the ratio of hydrostatic to effective stress, is controlled by the ratio between notch radius and specimen gauge radius, according to the work of Bridgman.[34] A schematic of the notched tensile specimen used in this investigation is shown in Figure 3, and the dimensions and associated

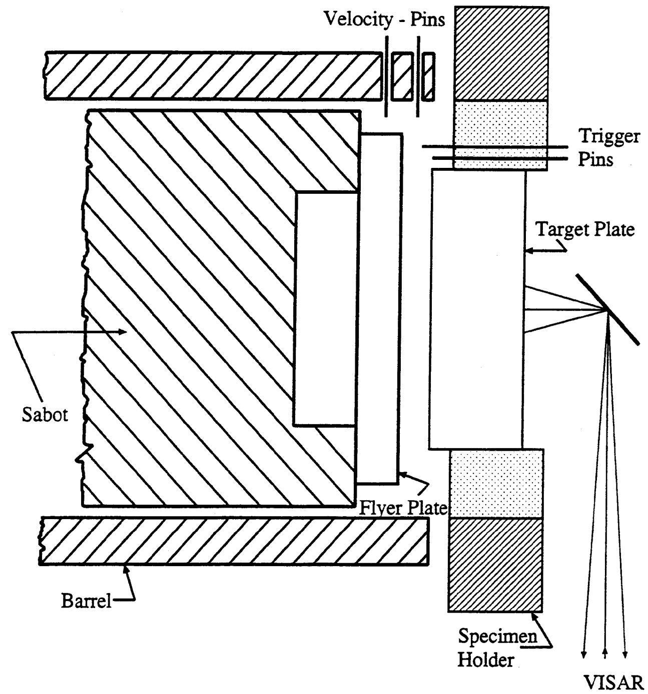

Fig. 4—Schematic of the plate impact experiments.

triaxiality levels are listed in Table I. The two notched profiles are similar to the C- and E-notch designations studied by Hancock and Mackenzie.[35]

In order to minimize rate effects between specimen geometries, the striker velocities were adjusted for each specimen or notch type to ensure that the tests were conducted at approximately the same diametral strain rate (Table I). Variations in strain rate will persist during each test because increases in load-carrying capacity due to work hardening and increases in gage length will both tend to reduce strain rate. In contrast, decreases in the load-carrying capacity due to a reduction in area or evolution of damage will increase strain rate. These effects are small, however, because the flow stress of brass is relatively rate insensitive for the range of strain-rate variation occurring in a typical TSHB experiment.

B. *Flyer Plate Impact*

Figure 4 is a schematic of the plate impact experiments in which a 50-mm-diameter, 8-mm-thick target plate is impacted by a 55-mm-diameter, 3-mm-thick flyer plate. The flyer plates are launched to velocities in the range of 53 to 256 m/s using a 75-mm-diameter gas gun. Upon impact,

Table I. Specimen Geometry and Experimental Conditions*

Specimen	Gage Radius (mm)	Notch Radius (mm)	Gage Length (mm)	Triaxiality (σ_{hyd}/σ)	Strain Rate (s^{-1})
C-notch	2.04	1.04	2.08	0.75 to 0.8	2600 to 3400
E-notch	2.04	3.18	6.35	0.5 to 0.6	1600 to 2100
Uniaxial	1.59	na	12.7	1/3	2200 to 2900

* (1) the notch gage length was taken as 2 times the notch radius for the purpose of calculating gage strain rate; and (2) triaxiality levels for the notched specimens were determined from the numerical calculations.

compressive shock waves are generated at the impact faces of the flyer and target plates. These compressive waves propagate towards the free surface of each plate where they reflect as tensile unloading waves that propagate back towards the interior of each plate. Due to the difference in thickness between the two plates, the two tensile unloading waves meet along a plane located 3 mm from the free surface of the target plate. The superposition of the unloading waves results in a state of extreme tensile triaxiality that can produce a spall layer through ductile fracture. The strain state is essentially uniaxial strain, and the level of stress is determined by the impact velocity. The difference between the impact velocity of the flyer plate and the velocity of the ejected spall layer is a measure of the material spall strength. Further details of the plate impact experiments for the specimens studied in this article are given by Nahme and Worswick.[22]

C. *Metallography*

Tensile test specimens and impacted plates were sectioned along their axis of symmetry parallel to the loading or impact direction. Special care was taken to prepare the metallographic specimens in a consistent fashion and to ensure flatness, a particularly difficult task with leaded brass because the soft lead had a tendency to smear out of the voids and render the brass matrix prone to edge rounding. The final polishing stage employed a vibratory technique to minimize rounding artifacts.

A digital image analysis system was used to analyze the porosity and aspect ratio of the lead particles and voids in the section planes. Optical microscope images were obtained with a CCD camera mounted on an inverted metallograph. Images were digitized using a standard 8-bit, 640×480 pixel frame-grabber mounted in a personal computer and then analyzed using an in-house computer program. The magnification used in the current study resulted in a pixel size of 0.625 μm with a corresponding field size of 400×300 μm. Standard error minimization techniques were applied, including corrections for variations in field illumination and frame averaging to reduce video noise. Particle/void detection was based on image segmentation techniques using a threshold gray scale level to distinguish between pixels assigned to particle/voids (dark) or matrix (light) material. Void/particle features such as individual feature size, shape, location, and orientation were recorded as well as the areal fraction and average feature aspect ratio for the entire field. Note that the particle/void areal fraction was taken as the volume fraction for the purposes of this study.

Images were acquired over the entire gage section of each notched specimen (Figure 3) on a regular grid pattern in order to examine spatial variations in damage. Local measures of porosity and aspect ratio were determined at the center and edge of the tensile specimens. These measures were determined as the average value over the central nine microscope fields and a three by two block of fields at the edge. Values of porosity and void aspect ratio acquired in this manner were used to construct histories of damage evolution from multiple specimens loaded to various strain levels. The standard deviations presented as error bars for these histories may be interpreted as the variance in the measured value over the area considered.

For the plate impact specimens, images were first acquired in a pattern three images wide running along the target plate centerline in order to locate the position of the incipient spall plane. Additional measurements, also three images wide, were acquired running along and perpendicular to the incipient spall plane. Variances were calculated using the three adjacent measurements for each position.

Local variations in lead particle spacing were considered using interparticle dilational spacing (IPDS) frequency spectra extracted from matrix erosion tessellations.[24,25] This image analysis technique "tessellates" the background (or matrix) of the image into regions "closest" to each particle. A process of progressive dilation of each particle is repeatedly applied until all particles have merged with their neighbors. Each particle dilation (or matrix erosion) pass is performed by adding a row of pixels to the perimeter of each particle. The boundaries at which particles "merge" are recorded along with the frequency of particles that merge with neighbors for each dilation pass. Once the dilation process is complete, the resultant boundaries define tessellation cells of pixels closest to the particle contained within each cell (Figure 5), and the IPDS frequency spectra can be used to discern the degree of clustering and characteristic cluster spacing(s) present in the particle field.[24,25] To improve the statistical significance of the IPDS statistics and to examine long-range cluster spacings, a series of overlapping images within the notched and plate specimens were first merged to obtain large-scale, high resolution particle fields prior to tessellation.

IV. DAMAGE MODEL

The quantitative metallographic data was used to assess a Gurson-based[26,27,28] model of ductile fracture, as implemented within the LSDYNA explicit dynamic finite element code.[30] For brevity, details of the constitutive formulation and numerical models of the experiments are omitted. The current implementation of the Gurson model is described in Reference 29, and the TSHB and plate impact simulations are described in References 21, 22, and 29.

One modification to the models in References 21, 22, and 29 was considered in the current work; that is, a stress-controlled void nucleation model was adopted rather than a strain-controlled approach. The goal in adopting a stress-controlled treatment was to account for the influence of triaxiality in reducing the plastic strain required to initiate voids. Following Gurson,[26] void nucleation is assumed to occur within a second-phase particle field at stress levels following a normal probability distribution. The rate of void nucleation is then given by

$$f_{\text{nucleation}} = \frac{f_N}{S_N\sqrt{2\pi}} \exp\left[-\frac{1}{2}\left(\frac{\sigma - \sigma_N}{S_N}\right)^2\right]\dot{\sigma} \qquad [1]$$

The term f_N represents the volume fraction of void nucleating particles while σ_N and S_N are the average and standard deviation of the stress levels at which particles nucleate voids. Adopting the approach taken by Argon *et al.*,[36] the stress acting on the particle field was taken as

$$\sigma = \bar{\sigma} + \sigma_{\text{hyd}} \qquad [2]$$

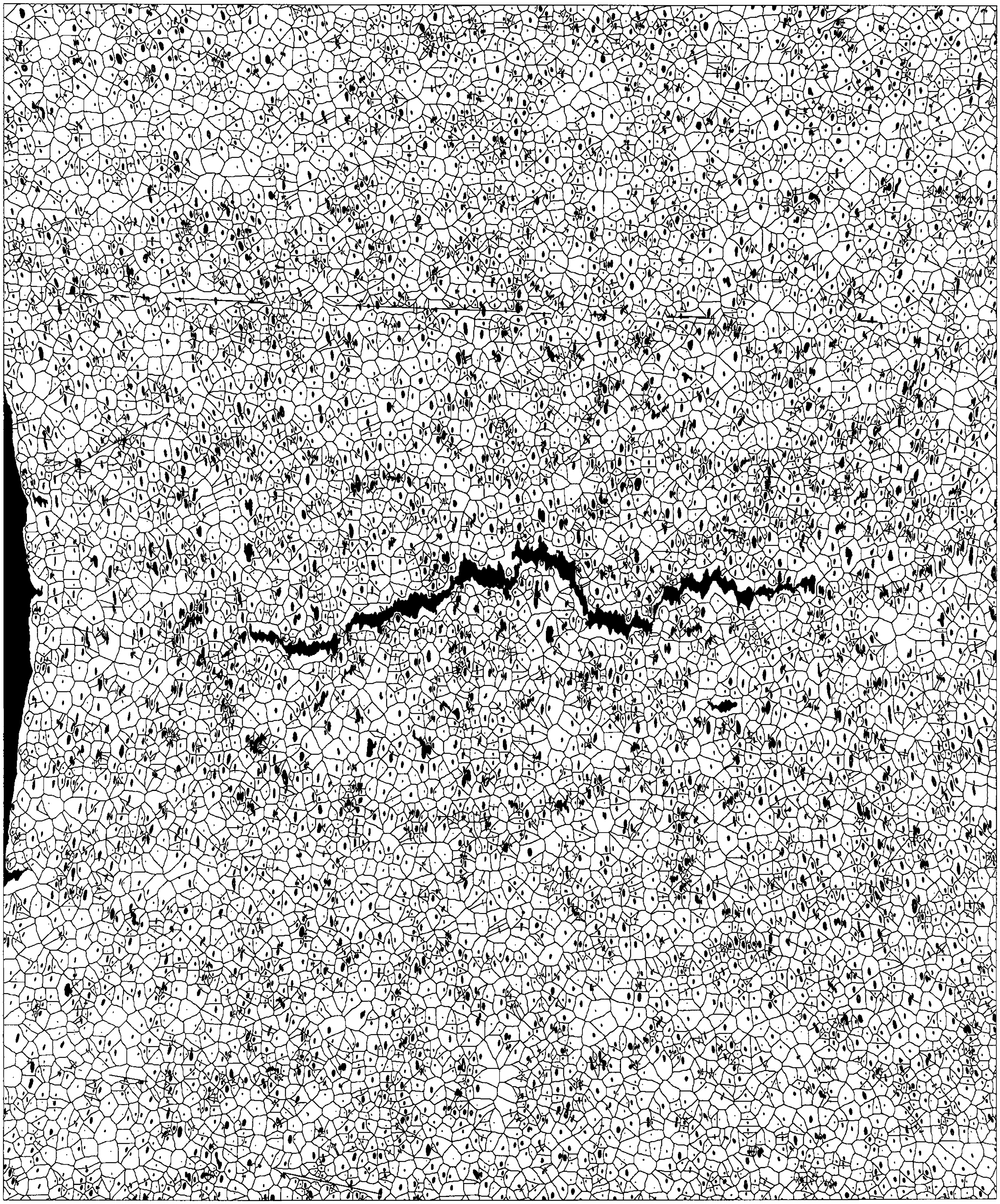

(*a*)

Fig. 5—Matrix erosion tessellations from notched TSHB specimens interrupted just prior to fracture: (*a*) E-notch ($\varepsilon_{\mathrm{True}} = 0.64$).

in which $\bar{\sigma}$ is the matrix flow stress and σ_{hyd} is the hydrostatic component of stress. With increased triaxiality, the ratio of hydrostatic stress to flow stress, the applied stress, σ, will increase and nucleation will occur at lower strains. Based

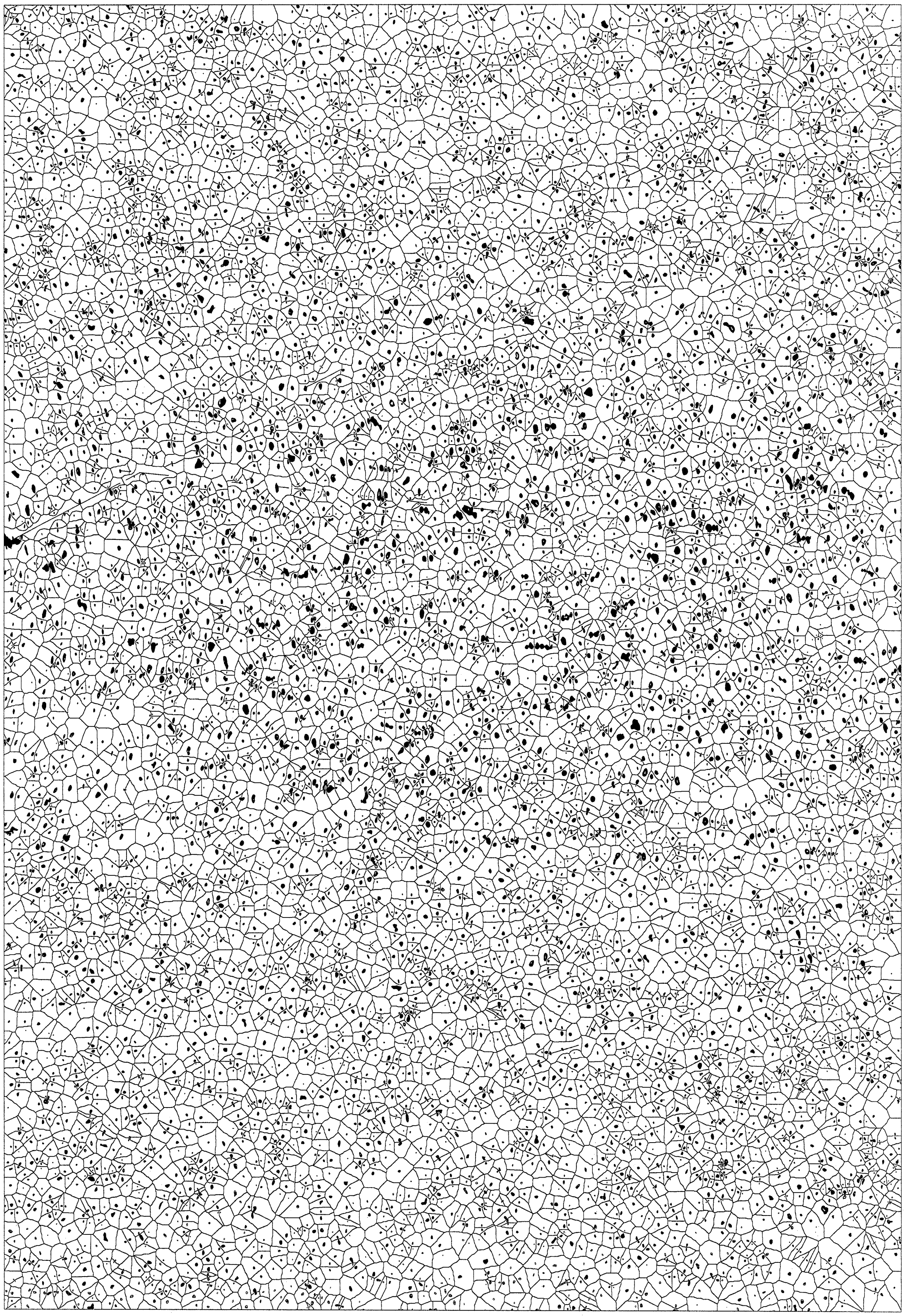

(*b*)

Fig. 5—Continued. (*b*) C-notch ($\varepsilon_{\mathrm{True}} = 0.32$).

upon the metallographic observations of void damage (discussed subsequently and in Reference 9) and the stress *vs* plastic strain behavior given in Reference 9, σ_N and S_N were set equal to 400 and 50 MPa, respectively.

V. EXPERIMENTAL RESULTS

A. *Mechanical Testing*

The high triaxiality C-notch specimens were found to fracture at a measured diametral strain of 59 pct while the intermediate triaxiality E-notch specimens fractured at 71 pct diametral strain. Figure 6 shows the stress-strain response from TSHB tests of the notched specimens tested to fracture as well as a uniaxial curve for which the specimen did not fail. Strain rates for these tests are given in Table I. The loading duration and intensity were not sufficient to produce fracture in the uniaxial specimens during the first incident pulse. The increase in stress level with notch severity that is evident in the data is caused by the increased constraint on plastic flow within the specimen gage region. This constraint leads to the increase in triaxiality at the specimen center (Table I) and resulting loss in ductility. Note that the true stress-strain data for the notched samples were converted from engineering stress-strain data using the finite element models to relate the change in specimen cross section to measured elongation. These predictions of specimen geometry were confirmed from physical measurements taken from tests interrupted prior to fracture. For the uniaxial samples, the diametral strain was determined from the axial elongation assuming volume constancy and uniform deformation within the gage section. Thus, the onset of necking was neglected in the uniaxial data, as reflected in Table I, which indicates a constant triaxiality of 1/3 for the uniaxial sample.

Measured spall strengths for the leaded brass plates were in the range of 1.14 to 1.25 GPa. Shock velocity-particle velocity diagrams and free-surface velocity time history data from all of the plate experiments performed on this material are discussed in detail in Reference 22. Free-surface velocity time history data for plates impacted at 93 and 175 m/s are presented in Section B.

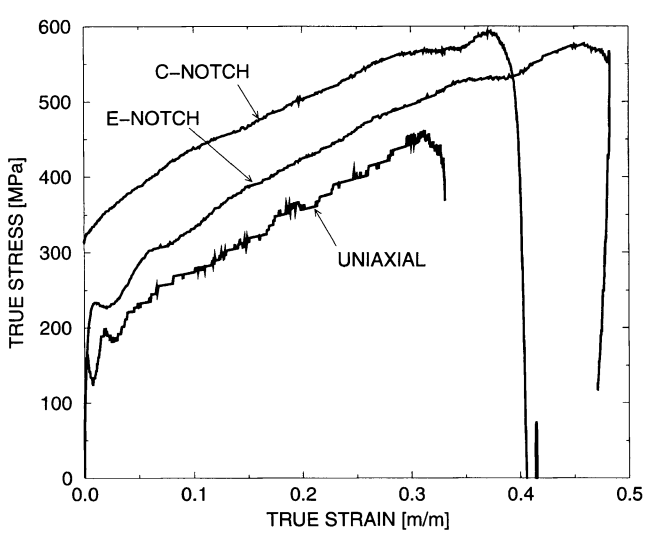

Fig. 6—Measured axial stress-strain response from the tensile tests.

B. *Damage Characterization*

1. *Hopkinson bar specimens*

Contour plots of void volume fraction and aspect ratio have been generated based on measurements acquired on a regular grid pattern within the gage regions of the notched specimens. The orientation of the grid pattern relative to the notch is shown in the schematic of Figure 3. Each "cell" in the plot represents the area of one microscope field, and the contours are based on the areal fraction within each cell. Figure 7 shows porosity distributions measured within E-notch specimens interrupted at strain levels between 0.20 and 0.64. For lower strains, void growth is most pronounced at the surface of the notch due to the local strain concentration Figures 7(a) and (b). As deformation continues, the porosity level at the specimen center surpasses that at the notch (Figure 7(c)) in spite of the strain concentration at the notch. The higher void growth rates at the center are due to the increased level of triaxiality in this region, a trend consistent with published models of void growth [6–8,26]. The aspect ratio is initially unity and increases to roughly 3 at the notch and 2.4 at the specimen center for a diametral strain of 0.64 (not shown). In contrast to the porosity trends, the void aspect ratio is larger at the notch than at the specimen center for the entire strain history. These results are again consistent with analytical predictions[7,8] for which the aspect ratio growth rate decreases with increased triaxiality. Note that while the central region of the E-notch specimen in Figure 7(c) was actually cracked, as shown in Figure 5(a), the pixels associated with the crack were not considered in calculating the porosity contours. Although suppression of the crack feature in this manner leads to an artificially low porosity level, the resulting porosity values are thought to be near to the critical value associated with onset of void coalescence.

The porosity distribution for the C-notch specimen interrupted at the largest strain of 0.32 is shown in Figure 8 and indicates that the rate of void expansion is more uniform across the width of the specimen compared to the E-notch results. This result is somewhat surprising because the triaxiality in the C-notch center is higher than for the E-notch, which exhibits higher porosity levels at the center compared to the notch. For the C-notch case, the elevated void expansion rates at the center are offset by the higher strain rates at the surface of the more severe C-notch. The increase in void aspect ratio for the C-notch was considerably lower than in the E-notch, due largely to the lower strain levels and higher triaxiality of the C-notch specimen.

All of the specimens exhibit local variations in porosity similar to that present in the undeformed material. Local "islands" of high porosity are particularly evident in Figures 7(b) and 8, for example, thereby suggesting that the lead particle fields are at least mildly clustered and that onset of fracture may be controlled by these clustered regions.

The porosity levels measured in the specimens interrupted at strain levels less than one third of the final fracture strain (Figure 7(a)) are close to the nominal lead fraction of 0.022. This observation suggests a threshold strain for void nucleation after which the porosity levels increase rapidly. Histories of void growth have been constructed based on measured porosities at the center of the notched specimens and are plotted as a function of diametral strain in Figure 9. Two values of void volume fraction are plotted; the closed symbols are from the central individual field, whereas the open

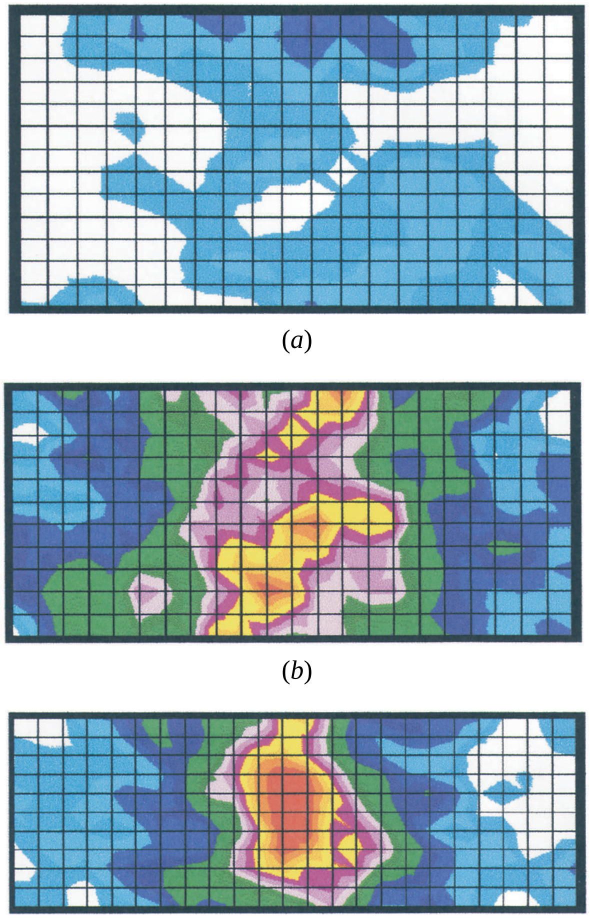

(*a*)

(*b*)

(*c*)

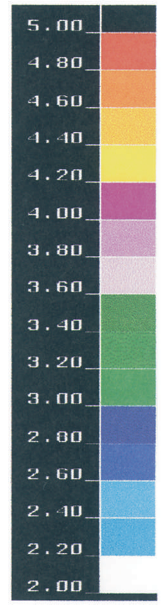

Fig. 7—Measured contours of porosity from E-notch specimens interrupted at diametral strains of (*a*) 0.2, (*b*) 0.45, and (*c*) 0.64. The plots are oriented such that the tensile straining direction is horizontal and the notches lie above and below the centers of each plot (Fig. 3.)

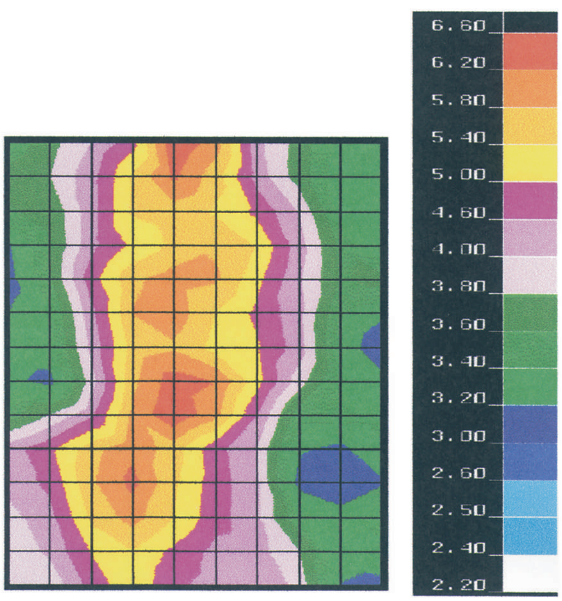

Fig. 8—Measured porosity contours for a C-notch specimen interrupted at diametral strain of 0.32.

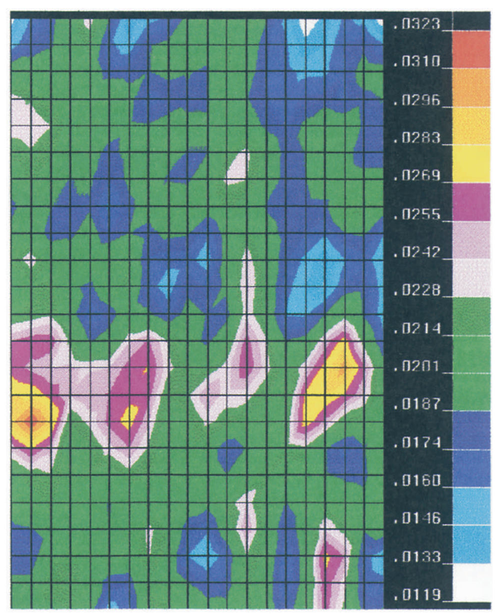

Fig. 11—Measured porosity contours from the center of the plate specimen. Impact face at top of plot.

symbols and error bars are average and standard deviation values from the central nine fields (*i.e.*, 3 3 3 grid). The data illustrate the higher void growth rates occurring within the higher triaxiality C-notch specimens in comparison to the intermediate triaxiality E-notch. No increase in porosity is observed beyond the measured standard deviation for the uniaxial specimen due to the lower triaxiality and its

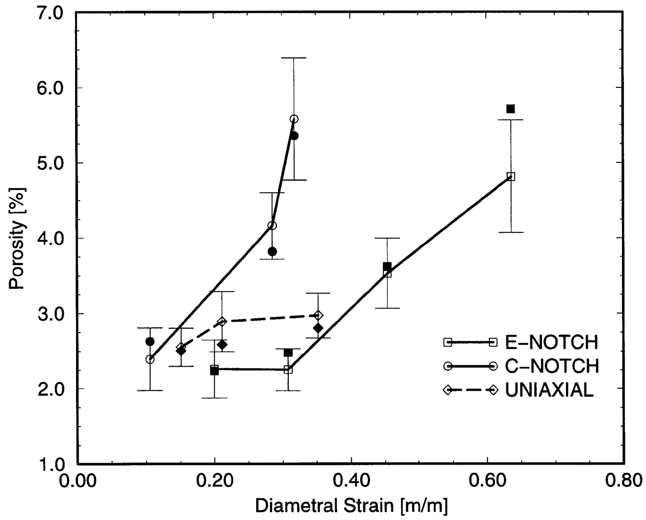

Fig. 9—Measured void volume fraction at the center of each interrupted TSHB specimen as a function of diametral strain.

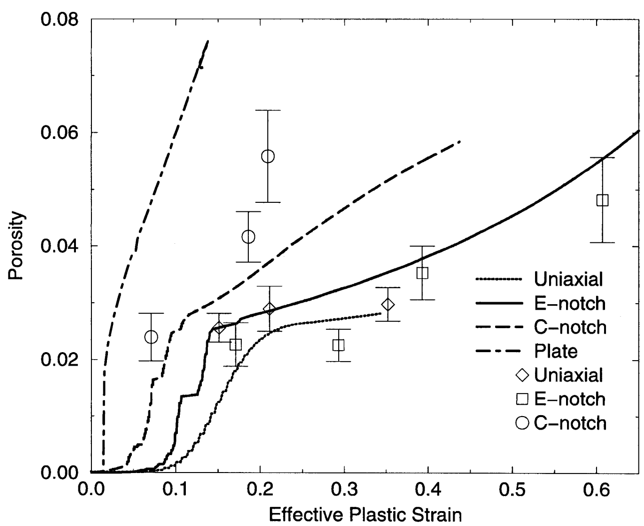

Fig. 10—Measured void volume fraction at the center of each specimen (symbols) as a function of corresponding effective plastic strain (at the center) determined from the finite element simulations. The curves are predicted porosity values from the numerical simulations of the TSHB and plate specimens.

associated lower void growth rate as well as a much larger void nucleation strain. Recalling that the initial lead particle fraction is approximately 0.022, it is evident from Figure 9 that a strain threshold exists for void nucleation, and that this nucleation strain decreases with increased triaxiality (notch severity).

The difference in growth rates between specimen types becomes more dramatic if one considers the local strains at the center of the specimens, which tend to be less than the bulk diametral values. To estimate the strain at the specimen centers, the finite element simulations were used to predict the effective plastic strain as a function of diametral strain for each notch geometry. Histories of void volume fraction *vs* effective plastic strain are shown in Figure 10 and reveal a dramatic increase in void growth rate with triaxiality. Predicted porosity histories using the Gurson-based constitutive model have also been plotted in Figure 10 for the TSHB and plate specimens. Note that the measurements detect areal fraction of both particle and void, whereas the predicted values only include void volume fraction of nucleated particles. Thus, the predicted curves start at the origin, whereas the measured values start at the initial particle faction of 0.022. The predicted curves display two damage growth rates evident for each specimen type. The higher initial growth rate can be attributed to the void nucleation phase of damage development. At porosity values of roughly 0.022, the majority of the particle field has nucleated voids, and the damage rate decreases to levels associated with void growth. As expected, the predicted slope associated with void growth becomes steeper with increased specimen triaxiality. The nucleation rates also increase with triaxiality while the strain level to initiate and complete void nucleation decreases with triaxiality, according to Eqs. [1] and [2]. The steps evident in the predictions for the TSHB specimens are due to sudden increases in stress level associated with the propagation of stress waves. In comparing the measured and predicted porosity levels, the predictions for the uniaxial and E-notch geometries agree well with the measured data, whereas the predicted growth rates for the C-notch appear too low.

2. *Plate impact specimens*

Plate impact experiments were performed with impact velocities in the range of 53 to 256 m/s. From examination of the free surface velocity response[18,19] and metallographic observations, it was evident that spallation or complete separation of the spall layer occurs for impact velocities in the range of 90 to 100 m/s. In an effort to capture an incipient spall plane, one experiment was performed at 93 m/s after the target and flyer plates were soft recovered for metallographic examination. Due to difficulties in controlling the test velocity within this range, only one specimen was recovered for study in this article. Mechanical testing results for other velocity levels and similar model materials are given in References 18 and 19.

The plate specimen impacted near the spall threshold was found to have discrete regions of higher porosity along the incipient spall plane. Contours of porosity from measurements taken at the center of the plate within the incipient spall layer are shown in Figure 11 and reveal a local band of high porosity. Periodic peaks exist in the porosity distribution along this band indicating regions of particle clustering as seen in the corresponding plots for the notched samples in Figures 7 and 8. The existence of this clustering may be due to the kinetics of the particle-coarsening heat treatment or may reflect the original solidification microstructure of the leaded brass rod.

Upon first inspection of the plates, the measured values of porosity near the center of the plate were significantly lower than the peak porosity levels measured in the notched specimens interrupted just prior to fracture. This result was surprising given that the plate impacted at 93 m/s was very near failure. Further metallographic examination revealed that the greatest amount of damage was situated away from the center line but near the outer edge of the plate. The high porosity in this region is due to the convergence of unloading or release waves from the impact surface, free surface, and circumferential surface of the specimen resulting in stronger triaxiality levels than at the specimen center. In fact, the

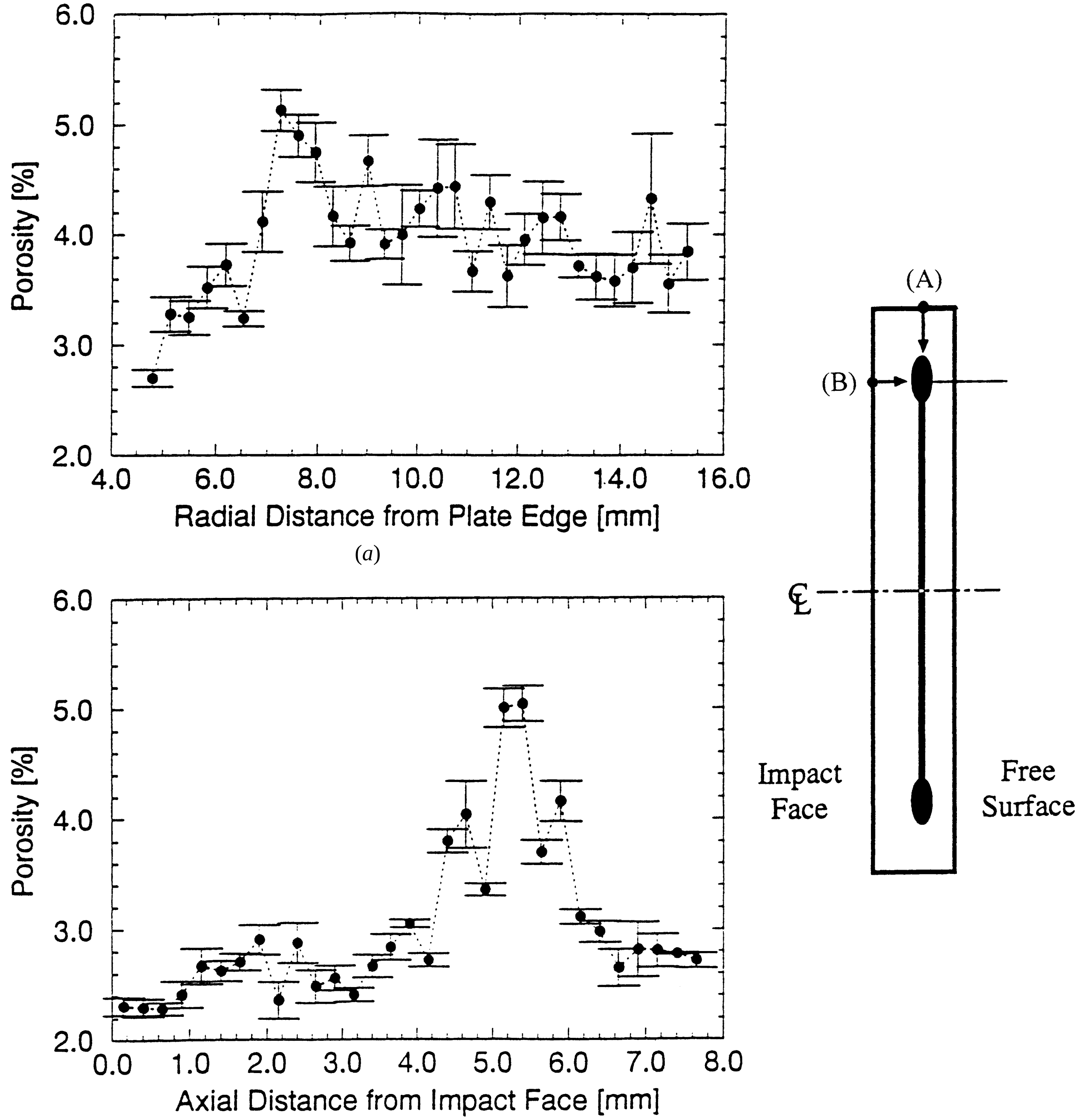

Fig. 12—Measured void volume fraction distributions (*a*) along a radial line within the spall layer starting at the outside edge of the plate and (*b*) along a line through the plate thickness running through the peak porosity zone.

model predicted that fracture would initiate in this region. The variation in porosity within the incipient spall plane was measured along a line starting at the outer edge of the plate, directed radially towards the center, and is plotted in Figure 12(a). Each value plotted is an average from three adjacent fields located within the spall layer while the error bars indicate the standard deviation on this average. The porosity near the outer edge is low, on the order of the lead volume fraction of 0.022. A peak porosity level of 0.054 was found approximately 7 to 7.5 mm from the edge of the plate. Moving away from this peak towards the plate center, the porosity distribution levels off to a band in the range of 0.035 to 0.045, similar to the levels seen at the plate center in Figure 11. Figure 12(b) shows the porosity distribution through the thickness of the plate along a line of constant radial distance from the plate center that intersects the peak porosity zone, as indicated in the schematic inset in Figure 12. The plot reveals that there is essentially no void growth outside of the incipient spall layer, and that the zone of damage is roughly 2 mm thick.

3. *Void coalescence conditions*

The maximum measured porosity levels are summarized in Table II for the notched TSHB specimens interrupted just

Table II. Maximum Porosity Levels Measured from Interrupted Specimens

Specimen	Triaxiality	Peak Porosity
E-notch	0.5 to 0.6	0.056
C-notch	0.75 to 0.8	0.048
Plate (93 m/s)	4 to 5	0.054

prior to failure as well as for the 93 m/s plate impact specimen with an incipient spall layer. Comparison of the conditions just prior to final fracture reveals a similar level of porosity in each case, suggesting that the critical porosity for catastrophic void coalescence is independent of triaxiality level, at least for the elevated triaxiality experiments considered herein. Note that failure did not occur in the low triaxiality, uniaxial specimens, and in other uniaxial experiments on this material, void coalescence is preceded by necking and a corresponding increase in triaxiality. It is possible that the lack of dependence between the critical porosity level for catastrophic void coalescence and triaxiality is due to the initially high volume fraction of second-phase particles and, therefore, may not apply to more dilute commercial materials. Nonetheless, the porosity levels in Table II provide a rational basis for the critical void coalescence criterion employed in Gurson–Tvergaard[26,27,28] continuum damage simulations for this material. Interestingly, similar levels of maximum porosity were found by Worswick and Pick[9] in quasi-static testing of notched specimens fabricated from the same type of model material. This comparison indicates that rate effects on void coalescence are not strong, at least for the fcc, strain-rate insensitive material under study.

The local sequence of void coalescence events leading to cracking can be observed in Figure 5. In Figure 5(b), extensive void growth has taken place as evidenced by the noticeably larger voids within the minimum section of the specimen. Void coalescence has also begun within closely spaced groups of particles, referred to as clusters. The mechanism of coalescence appears to be either void impingement and/or localized shearing. The E-notch sample in Figure 5(a) was interrupted much closer to final fracture; hence, a large crack has formed. Within and near the crack, coalesced void clusters are evident and the coalescence mode within clusters is similar to that in Figure 5(a). Large crack formation, however, occurs through linking of coalesced clusters, often through formation of shear bands that are evident between particle clusters at angles near 45 deg to the tensile straining axis.

Figure 13 shows IPDS spectra from undeformed material as well as from the samples shown in Figure 5. All three spectra show initial peaks in particle dilational spacings of roughly 10 μm. This spacing level corresponds to the characteristic interparticle spacing within so-called first-order clusters[24,25] and is of importance in the early stage of void coalescence occurring between nearest neighbors within clusters. A second peak can be discerned at roughly 20 μm. This so-called second-order cluster peak corresponds to the intercluster spacing and is of relevance in cluster-to-cluster linking.

In comparing the IPDS spectra for the undeformed and E-notch sample, it is evident that the E-notch spectrum exhibits higher frequencies of closely spaced particles ($<$10 μm). This statistical reduction in particle spacing is attributed to void growth within clusters, producing very closely spaced voids and favoring coalescence through void impingement. Visually, the reduction in void spacing can be observed in Figure 5(a). This trend is less evident in the C-notch sample (Figure 5(b)); however, this test was clearly interrupted much earlier in the final fracture process than the E-notch sample. Interestingly, the first- and second-order cluster spacings are considerably smaller than the spacings of the porosity "islands" evident in Figures 7, 8, and 11. This outcome suggests that the very final stage of fracture is dependent upon void cluster spacings beyond the orders identified in the IPDS data of Figure 13.

4. *Influence of critical porosity level on spallation*

The peak porosity data in Table II indicate that void coalescence leading to final fracture occurs for porosity levels in excess of 5.5 pct. The actual porosity at coalescence is difficult to determine; however, finite element simulations of plate impacts were performed in which the critical porosity level was varied parametrically to determine its influence on predicted spallation behavior. Two impact velocities were considered: 93 m/s for which spallation did not result and 175 m/s that resulted in the formation of a spall layer.[21,22]

Figures 14(a) and (b) compare the measured free-surface velocity time histories with FEM predictions using a range of critical void volume fraction levels, f_c, for the two impact velocities of 93 and 175 m/s, respectively. While detailed interpretation of the free-surface velocity histories are given in Reference 22, the material spall strength is determined experimentally, based on the drop in velocity in Figure 14(b) from the peak of 175 m/s to roughly 130 m/s over the period of 3.5 to 5 μs after impact. The subsequent oscillations are due to ringing of stress waves within the ejected spall layer. In Figure 14(a), spallation did not occur as indicated by a dramatic drop in velocity to nearly zero and an increase in the period of ringing that occurs within the intact (albeit damaged) 8-mm plate rather than a 3-mm spall layer.

The curves in Figure 14(a) indicate that spallation is predicted for values of f_c less than 0.08. Above this value, the porosity that accumulates within the damage layer does not cause separation of the spall layer. In Figure 14(b), the velocity drop associated with spallation is seen to increase with increasing values for f_c; that is, predicted spall strength increases with f_c. The magnitude of the predicted velocity drop for $f_c = 0.08$ agrees reasonably well with that of the measured curve. Subtle differences exist, however, between the measured and predicted response for both impact velocities. These differences may be due to over-prediction of the rate of damage accumulation within the model. In Figures 11 and 12(a), the measured porosity within the spall layer away from the plate edge is in the range of 3.5 to 4.5 pct and is considerably less than the predicted levels shown in Figure 9. This comparison demonstrates that the high triaxiality predicted growth rates are too high at the plate center, which are likely caused by the assumption of zero material viscosity inherent in the Gurson-based constitutive model. Future work will consider the incorporation of viscosity effects, as in References 18 through 20, because they can play a strong role in limiting damage evolution for the range of strain rates occurring within the plate specimens. It is unlikely that viscosity will affect the TSHB results

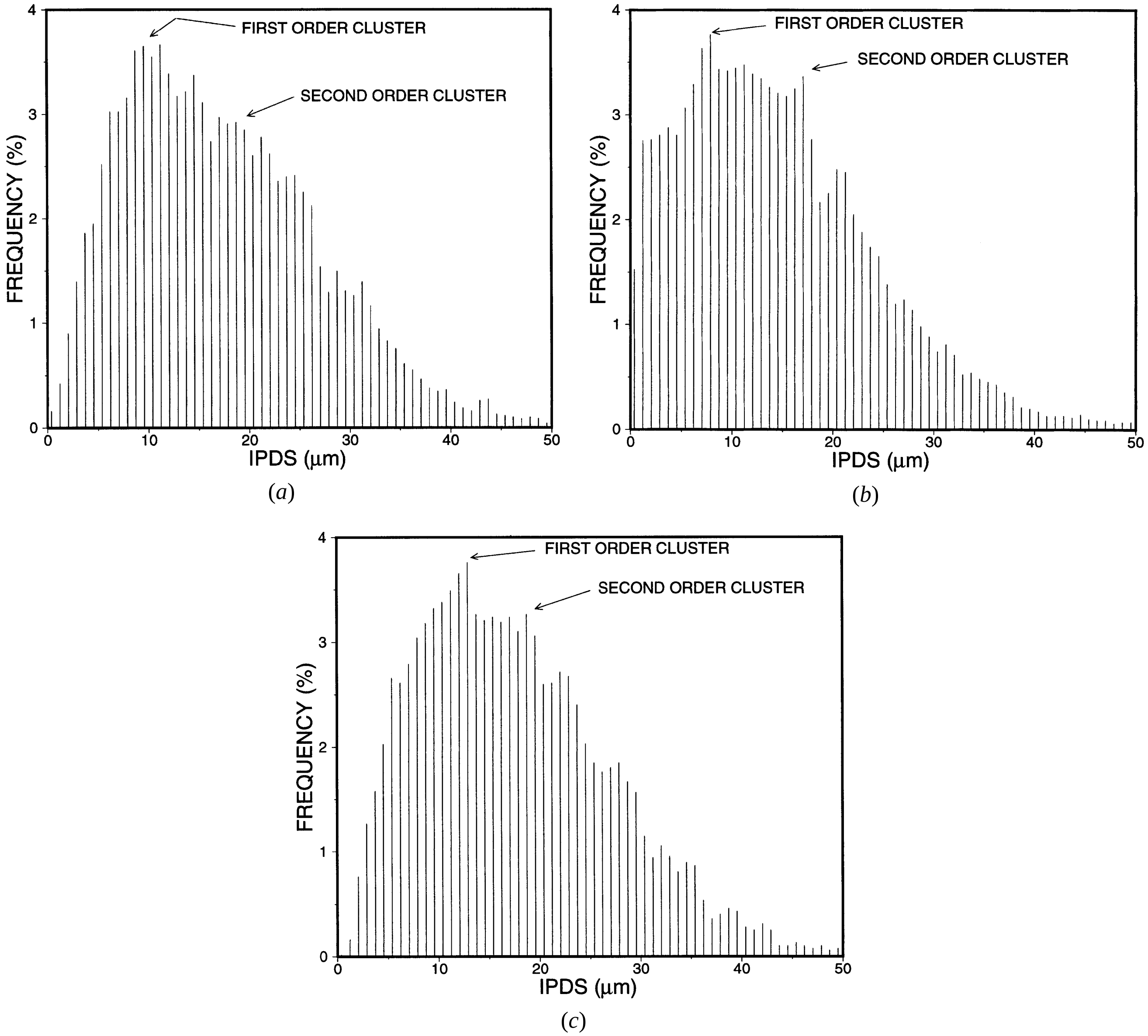

Fig. 13—Measured IPDS spectra from (*a*) undeformed sample, (*b*) E-notch specimen interrupted at 0.64 diametral strain, and (*c*) C-notch specimen at 0.32 diametral strain.

because these samples experience strain rates that are one to two orders of magnitude lower than in the plates.

VI. DISCUSSION

The present study has provided insight into the nature of damage nucleation, growth, and coalescence under high rate-deformation conditions for the model material studied. Interestingly, the conditions at void coalescence were similar for all three specimen types that fractured, thereby supporting the use of a failure criterion that incorporates a critical level of porosity for catastrophic void coalescence. It should be emphasized, however, that this result may be due to the high initial particle fraction considered. Such a void coalescence criterion may not apply in commercial materials where particle volume fractions are typically more dilute.

The stress-controlled nucleation approach introduced in the current Gurson-based FEM model effectively captures the reduction in void nucleation strain with increased triaxiality observed in the measured damage within the notched TSHB specimens. The predicted rates of void growth agreed with the experimental data for the lower triaxiality E-notch specimens but appeared too low in comparison with the C-notch results. In contrast, the growth rates for the high rate, high triaxiality plate impact specimens are found to be lower than that of the model. This contradiction likely results from the omission of viscous effects[18,19,20] that are likely to retard void-expansion rates within the plate specimens. In addition, numerical simulations of damage are known to be extremely sensitive to element size and mesh design. Thus, differences in meshing of each specimen may have led to inconsistencies in predicted damage rates. Current research[37] is considering the use of nonlocal damage formulations that are designed to control mesh sensitivity. In spite of the reported inconsistencies between the predictions and measured damage, the model does capture the trends in damage rates and fracture

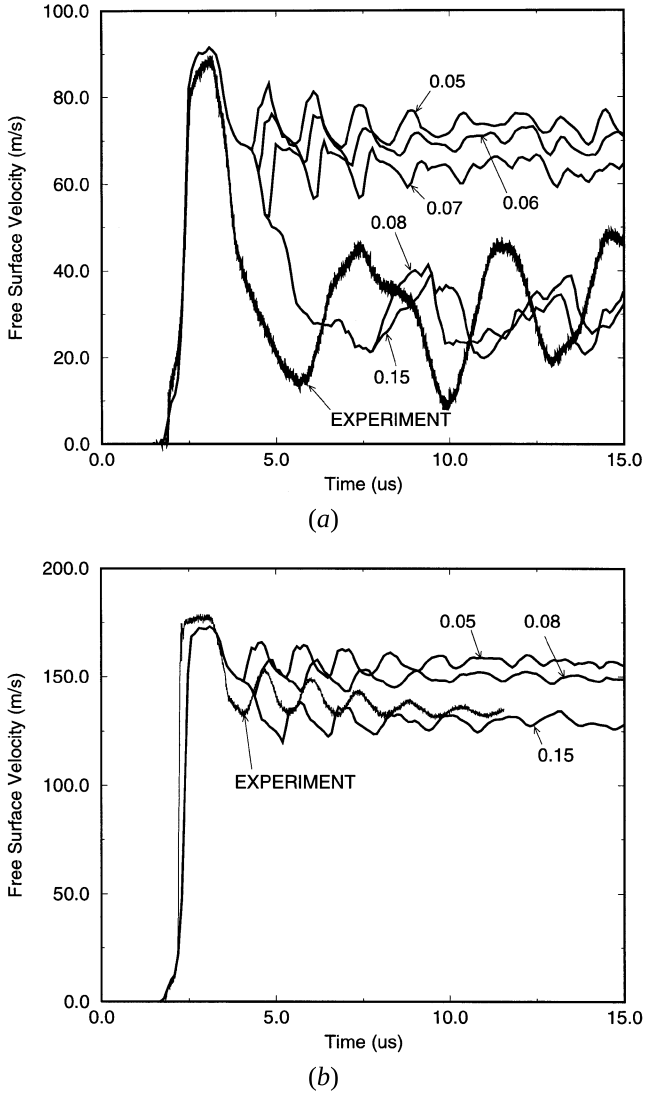

Fig. 14—Free surface velocity measurements and predictions for plate impact experiments at (*a*) 93 m/s and (*b*) 175 m/s. The critical void volume fraction to initiate void coalescence, f_c, is indicated for each predicted curve.

initiation quite well and represents a useful engineering tool for predicting fracture under high strain-rate conditions.

The IPDS spectra indicate subtle shifts in the interparticle and intercluster spacings with deformation. As voids grow and begin to link, the frequency of small separation distances increases, thereby allowing coalescence to initiate and propagate catastrophically across the specimen. Recent damage percolation studies in Al-Si alloys[38] have revealed that once coalescence occurs within several closely spaced void clusters, an unstable chain reaction of coalescence events produces large macrocracks without further bulk straining. Ongoing research is considering the application of damage percolation models to the current experiments.

VII. CONCLUSIONS

1. Catastrophic void coalescence occurs in the leaded brass model material studied for porosity levels in the range of 5.5 to 8.0 pct.
2. Damage rates predicted using the Gurson-based FEM model capture the trends observed in the TSHB and plate impact experiments; however, errors in growth rates exist for the higher triaxiality specimens.
3. The stress-controlled nucleation treatment accurately captures the experimentally observed dependence of nucleation strain on triaxiality.

ACKNOWLEDGMENTS

Financial support for this research was provided by the Natural Sciences and Engineering Research Council, the Canadian Department of National Defence, and SNC Industrial Technologies Incorporated. The authors thank Mr. P. Pelletier, SNC Industrial Technologies Incorporated, and Mr. P.J. Gallagher, Defence Research Establishment Suffield, for their support of this research.

REFERENCES

1. H.C. Rogers: *Trans. TMS-AIME*, 1960, vol. 218, pp. 498-506.
2. S.H. Goods and L.M. Brown: *Acta Metall.*, 1979, vol. 27, pp. 1-15.
3. D.R. Curran, L. Seaman, and D.A. Shockey: *Phys. Rep.*, 1987, vol. 147, pp. 253-88.
4. J.R. Fisher and J. Gurland: *Met. Sci.*, 1981, vol. 15, pp. 185-202.
5. R.J. Bourcier, D.A. Koss, R.E. Smelser, and O. Richmond: *Acta Metall.*, 1986, vol. 34, pp. 2443-53.
6. J.R. Rice and D.M. Tracey: *J. Mech. Phys. Solids*, 1969, vol. 17, pp. 201-17.
7. B. Budiansky, J.W. Hutchinson, and S. Slutsky: in *Mechanics of Solids, The Rodney Hill Anniversary Volume*, H.G. Hopkins and M.J. Sewell, eds., Pergamon Press, Oxford, United Kingdom, 1982, pp. 13-45.
8. M.J. Worswick and R.J. Pick: *J. Mech. Phys. Solids*, 1990, vol. 38, pp. 601-25.
9. M.J. Worswick and R.J. Pick: *J. Appl. Mech.*, 1991, vol. 58, pp. 631-38.
10. E.M. Dubensky and D.A. Koss: *Metall. Trans. A*, 1987, vol. 18A, pp. 1887-95.
11. Sun Jun: *Eng. Fract. Mech.*, 1991, vol. 39, pp. 799-805.
12. J. Pan, M. Saje, and A. Needleman: *Int. J. Fract.*, 1983, vol. 21, pp. 261-78.
13. M.J. Worswick, N. Qiang, P. Niessen, and R.J. Pick: *Shock Wave and High-Strain-Rate Phenomena in Metals*, M.A. Meyers, L.E. Murr, and K.P. Standhammer, eds., Dekker, New York, NY 1990, pp. 87-95.
14. C.R. Mason, M.J. Worswick, and P.J Gallagher: *J. Phys.*, 1997, vol. 7, pp. C3-827-C3-832.
15. I.M. Fyfe and A.M. Rajendran: *J. Appl. Mech.*, 1982, vol. 49, p. 31.
16. L. Seaman, D.R. Curran, J.B. Aidun, and T. Cooper: *Nucl. Eng. Des.*, 1987, vol. 105, pp. 35-42.
17. M.J. Worswick and R.J. Pick: *Mech. Mater.*, 1995, vol. 19, pp. 293-309.
18. M.M. Carroll and A.C. Holt: *J. Appl. Phys.*, 1972, vol. 43, pp. 1626-36.
19. J.N. Johnson: *J. Appl. Phys.*, 1981, vol. 52, pp. 2812-25.
20. F.L. Adessio and J. Johnson: *J. Appl. Phys.*, 1993, vol. 74, pp. 1640-48.
21. M.J. Worswick, H. Nahme, and J. Clarke: *DYMAT J.*, 1994, vol. 1, pp. 229-44.
22. H. Nahme and M.J. Worswick: *Proc. EuroDymat '94*, Oxford, United Kingdom, Sept. 26–30, 1994, pp. C8-707-C8712.
23. S. Nemat-Nasser, J. Issacs, and J. Starret: *Proc. R. Soc. A*, 1991, vol. 435, p. 371.
24. M.T. Shehata and J.D. Boyd: *Inclusions and their Influence on Materials Behaviour*, ASM INTERNATIONAL, Metals Park, OH, 1988, pp. 123-31.
25. A.K. Pilkey, M.J. Worswick, C.I.A. Thomson, D.J. Lloyd, and G. Burger: *Adv. Ind. Mater.*, D.S. Wilkinson, W.J. Poole, and A. Alpus, eds., The Metallurgical Society of CIM, 1998, pp. 105-21.
26. A.L. Gurson: *J. Eng. Mater. Technol.*, 1977, vol. 99, pp. 2-15.
27. V. Tvergaard: *Int. J. Fract.*, 1981, vol. 17, pp. 389-407.
28. V. Tvergaard and A. Needleman: *Acta Metall.*, 1984, vol. 32, pp. 157-69.
29. M.J. Worswick and P. Pelletier: *Eur. J. Phys., Appl. Phys.*, 1998, AP4 pp. 257-67.

30. LS-DYNA3D, *Nonlinear Dynamic Analysis of Structures in Three Dimensions*, Livermore Software Technology Corp., Livermore, CA, 1994.
31. J. Harding, E.D. Wood, and J.D. Campbell: *J. Mech. Eng. Sci.*, 1960, vol. 2, pp. 88-96.
32. H. Kolsky: *Proc. R. Soc. A*, 1949, vol. 62, pp. 676-700.
33. B. Hopkinson: *Phil. Trans. A*, 1914, vol. 213, pp. 437-56.
34. P.W. Bridgman: *Studies in Large Plastic Flow and Fracture*, McGraw-Hill, New York, NY 1952.
35. J.W. Hancock and A.C. Mackenzie: *J. Mech. Phys. Solids*, 1976, vol. 24, pp. 146-69.
36. A.S. Argon, J. Im, and R. Safoglu: *Metall. Trans. A*, 1975, vol. 6A, pp. 825-37.
37. A.K. Kamel, M.J. Worswick, and D. Nandall: *Effect of Non-Local Damage Treatment on Dynamic Fracture Predictions*, Proc. ASME PVP Congr., San Diego, CA, July 1998.
38. M.J. Worswick, A.K. Pilkey, C.I.A. Thomson, D.J. Lloyd, and G. Burger: *Microstructural Science Analysis of In-Service Failures and Advances in Microstructural Characterization, Proc. of the 31st Annual Technical Meeting of the International Metallographic Society*, 26-29 July, 1998, Ottawa, Ontario, Canada, ASM International, vol. 26, pp. 507-14.